


# Characterization and discrete element simulation of grading and shape-dependent behavior of JSC-1A Martian regolith simulant

Zhengshou Lai<sup>1</sup> · Qiushi Chen<sup>1</sup> 

Received: 9 April 2017  
© Springer-Verlag GmbH Germany 2017

**Abstract** Granular regolith simulants have been extensively used in the preparation of space missions to test rovers and scientific instruments. In this work, the physical and mechanical properties of the JSC-1A Martian regolith simulant (MRS) are characterized using conventional and advanced laboratory techniques. Particle images are obtained using X-ray computed tomography, from which particle shapes are characterized through a series of imaging processing techniques and are further used to generate irregularly-shaped numerical particles. The characterized particle size distribution and irregularly-shaped numerical particles are incorporated into a discrete element model to simulate grading and shape-dependent behavior of the JSC-1A MRS. The developed discrete element model is calibrated and validated against laboratory direct shear tests. Simulations without the consideration of particle shapes and simulations with a rolling resistance contact model are also performed to investigate the effect of particle shapes on the behavior of the JSC-1A MRS.

**Keywords** Martian regolith simulant · Discrete element method · Particle size distribution · Particle shape · X-ray computed tomography · Direct shear test

## 1 Introduction

Martian regolith simulant (MRS) is an analogue developed using terrestrial soils based on the current understanding of real Martian regolith. It provides a preview of the physi-

cal environment an exploration rover may encounter in a space exploration mission. The understanding of regolith properties and the ability to predict regolith behavior would help guide the design of rovers, minimize the risk of sinkage and slippage during rover maneuver, and provide constraints for geomorphological modeling [1–3]. Moreover, a thorough understanding of regolith properties are needed to develop new regolith-based materials for functional building blocks for future infrastructure needs on Mars [4–7]. There has been continuous research to develop different MRS for various applications. Table 1 summarizes a non-exclusive list of currently developed MRS worldwide that are suitable for physical and mechanical experiments.

MRS consists mostly of irregularly-shaped particles of various sizes. To accurately model and predict their behavior, it is important to realize that the information pertaining to such material behavior is fundamentally encoded at the grain scale [14–16]. In the context of mechanical responses, two of the most salient factors are the particle size distribution (i.e., grading) and particle shapes. The micromechanics-based discrete element method (DEM) [17] is ideally suited to capture those salient features of granular materials from a fundamental level.

In the context of modeling MRS, Hopkins and co-workers [18, 19] are among the first researchers to develop DEM-based numerical models to simulate the soil-rover behavior and soil digging in regolith simulant. Non-spherical particle shapes are accounted for using polyhedral grains having basic shapes. In [20], a three-dimensional DEM is used to simulate regolith behavior in triaxial tests and interactions with a rover wheel. The particle shape is found to be a crucial factor in the simulated regolith behavior, and the use of ellipsoid and poly-ellipsoid particle shapes improved agreement between simulation and experiment. In a more

✉ Qiushi Chen  
qiushi@clemson.edu

<sup>1</sup> Glenn Department of Civil Engineering, Clemson University, Clemson, SC 29634, USA

**Table 1** Currently developed Marian regolith simulants suitable for physical and mechanical experiments

Type	Description	Location	References
JSC-1A	Glassy volcanic ash and cinders	Hawaii, US	[8]
ES-1	Fine dust	Nepheline Stjernoy, UK	[9, 10]
ES-2	Fine aeolian sand	Red Hill, UK	[9, 10]
ES-3	Coarse sand	Leighton Buzzard, UK	[9, 10]
MMS	Basalt crushing	California, US	[11]
Scott	Banks Peninsula basalts	South Island, New Zealand	[12]
JMSS-1	Basalt crushing, magnetite and hematite	Jining and Hebei, China	[13]

recent work [21], a tri-sphere particle clump is developed to account for the particle interlocking effects and is used within a mono-dispersed particle assemblies to simulate MRS. As an alternative approach to account for particle shape effect, a rolling resistance contact model is integrated into the DEM model to simulate wheel–soil interaction over rough terrain [22]. Although different types of non-spherical or non-disc particle shapes have been used in previous studies, the effects of realistic particle shapes and particle size distribution have yet to be included and will be the focus of this work.

In this work, physical and mechanical properties of JSC-1A MRS are characterized by a series of laboratory tests. Of particular interests are the particle size distribution and realistic particle shapes. X-ray computed tomography is used to obtain particle images, from which particle shape data is obtained and used in constructing irregularly-shaped particles. Grading and shape-dependent DEM model are developed to simulate and predict the behavior of JSC-1A MRS, which is among the first efforts to incorporate the realistic particle size distribution and particle shapes into a numerical model to simulate the behavior of MRS.

## 2 Laboratory tests on JSC-1A Martian regolith simulants

A series of laboratory tests are conducted to characterize the physical and mechanical properties of JSC-1A MRS. The type of JSC-1A MRS used in this work has particle sizes smaller than 5 mm and is distributed by Orbital Technologies Corporation. The JSC-1A MRS is a natural earthen material obtained from volcanic ashes. It approximates, within the limits of current understanding, the reflectance spectrum, mineralogy, chemical composition, particle size, density, porosity, and magnetic properties of the oxidized soil of Mars [8]. It is well suitable to help understand the mechanical behavior of real Martian regolith. In addition, as the MRS is actually an earthen material, the framework and findings from this work could be applied to other earthen soils.

**Table 2** Laboratory tests conducted and the corresponding ASTM standards

Test	ASTM standard
Specific gravity	ASTM D854-14
Sieve analysis	ASTM D422-63
Hydrometer analysis	ASTM D422-63
Atterberg limits analysis	ASTM D4318-10
USCS soil classification	ASTM D2487-11
Direct shear test	ASTM D3080-11

### 2.1 Characterization of physical and mechanical properties

Table 2 lists laboratory tests conducted in this study and the corresponding ASTM standards to characterize the physical and mechanical properties of the JSC-1A MRS.

The specific gravity of the JSC-1A MRS is measured to be  $1.94 \pm 0.02$ . The maximum particle size of the soil sample is 5 mm, and the mean particle size is 0.41 mm. The particle size distribution will be detailed and further characterized in a subsequent section. The coefficient of uniformity  $C_u$  and the coefficient of gradation  $C_c$ , based on Eqs. (1) and (2), are calculated to be 20.77 and 1.42, respectively.

$$C_u = \frac{D_{60}}{D_{10}} \quad (1)$$

$$C_c = \frac{(D_{30})^2}{D_{10} \times D_{60}} \quad (2)$$

where  $D_{10}$ ,  $D_{30}$ , and  $D_{60}$  are the particle diameters corresponding to 10, 30, and 60% finer in the particle size distribution curve, respectively.

Atterberg limit analysis shows that the fine content of the simulant is non-plastic. Based on the above information, the JSC-1A MRS is classified as well-graded sand (SW) following the Unified Soil Classification System (USCS). The bulk unit weight of the simulant is estimated from specimens of the direct shear test, and its value is evaluated to be  $934 \pm 30 \text{ kg/m}^3$ .

## 2.2 Characterization of shear strength

Shear strength parameters of the MRS are characterized through the direct shear test (ASTM D3080-11). The specimen in the direct shear test is a cylindrical shape with a diameter of 63.5 mm (i.e. 2.5 inches) and a height of 25.4 mm (i.e. 1.0 inch). During preparation, the specimen is vibrated and slightly compacted with a pestle to remove the potential cavity and to improve the sample homogeneity. The specimen is firstly consolidated with specified confining pressure. Three levels of nominal confining stress are considered: 95.8, 191.5, and 383.0 kPa (i.e. 2,000, 4,000 and 8,000 psf). After consolidation, the specimen is sheared at a rate of 0.254 mm/min by applying a lateral displacement to the lower part of the shearing cell. For each level of confining stress, three specimens are prepared and tested. The averaged responses are reported and will be used to calibrate and validate numerical models.

The stress and normalized shear (lateral) displacement relations are shown in Fig. 1a. The normalized shear displacement is the ratio of the lateral displacement of the lower part of the shear cell to its diameter. The actual contact area between the upper and lower shearing cell is used in the calculation. From the figure, it can be seen that there is no notable reduce of the shear stress after the peak value. As shown in Fig. 1b, at a low or medium normal stress (i.e., 95.8 and 191.5 kPa), the specimen exhibits a dilative behavior. This dilative behavior is suppressed under high normal stress (383 kPa). The volumetric strain starts to decrease after the peak shear stress. This phenomenon may be contributed by the breakage of the large particles that leads to a reduction in the overall volume.

The maximum friction angle is determined by fitting the test data in the maximum shear stress vs. normal stress plot, as shown in Fig. 2a. For the JSC-1A MRS, the maximum friction angle is found to be  $41.4^\circ \pm 2.2^\circ$ . There is a very small cohesion strength of 94 psf, which will be neglected in this study. For the calculation of dilation angle, the following definition is adopted [23]

$$\tan \psi = -\frac{\dot{\epsilon}_{yy}}{\dot{\epsilon}_{xy}} = \frac{dv}{du} \quad (3)$$

where  $\dot{\epsilon}_{yy}$  and  $\dot{\epsilon}_{xy}$  are the time derivative of the  $yy$  (vertical) and  $xy$  (shearing) components of the strain tensor, respectively;  $dv$  and  $du$  are incremental vertical and shear displacement, respectively. Figure 2b shows the maximum angle of dilation evaluated by Eq. (3) for all three normal stresses.

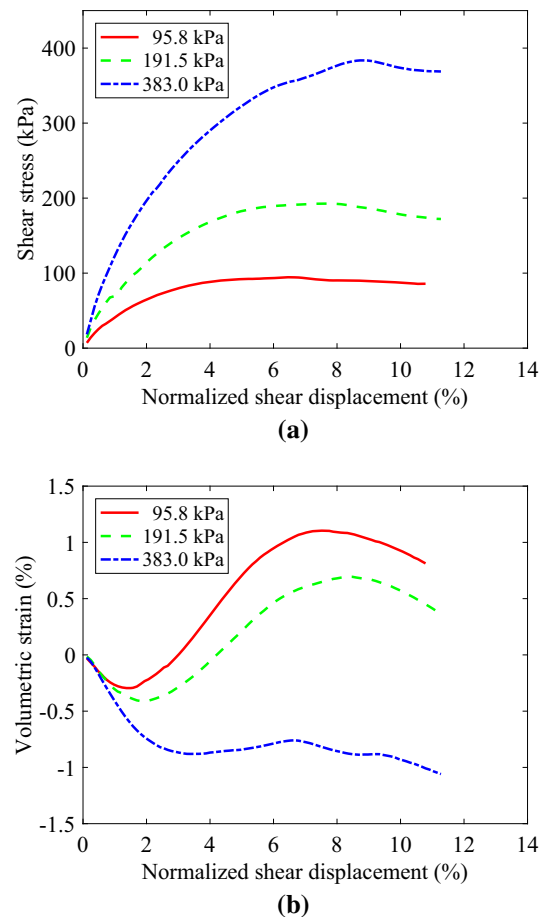


**Fig. 1** Results of laboratory direct shear test on JSC-1A MRS: **a** shear stress versus normalized shear displacement, **b** volumetric strain versus normalized shear displacement

## 3 Characterization of particle size distribution

In this section, details on characterization and modeling of particle size distribution are presented. In the sieve analysis, the following sieves are used: No. 4, 10, 20, 40, 60, 100, and 200. Hydrometer analysis is used to further characterize the size distribution for the fraction that is finer than the No. 200 sieve size (0.075 mm). The resulting particle size distribution curve is shown in Fig. 3a.

The particle size distribution data obtained from laboratory tests could be fitted through distribution models. In this work, the Rosin–Rammler (RR) distribution model is adopted [24]. A new form of the cumulative distribution function is proposed in this work that modifies a previous version [25] to use the mean particle size as a model parameter. The modified form of the RR model is given as

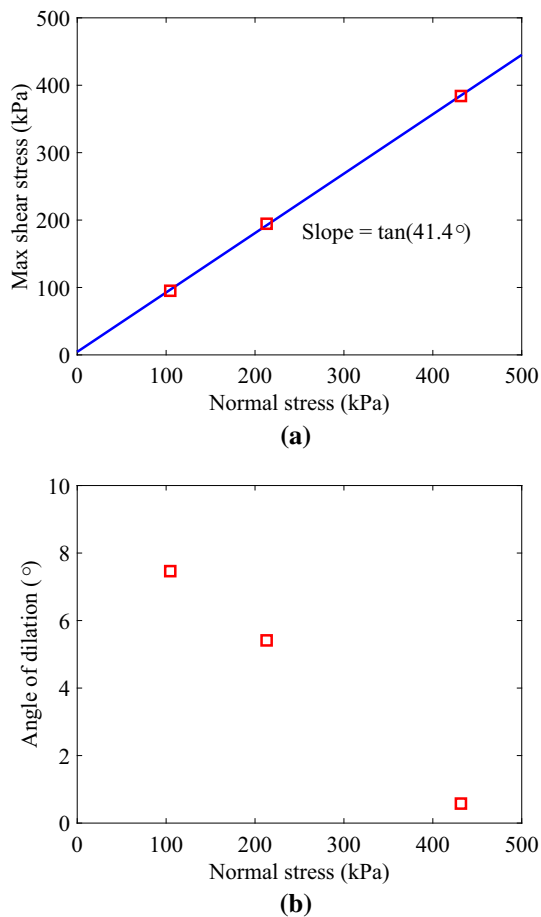


**Fig. 2** Maximum friction and dilation angles evaluated from laboratory direct shear tests: **a** maximum shear versus normal stress; **b** maximum dilation angle

$$F(x) = 1 - \exp(\log(0.5)(x/D_{50})^\beta) \quad (4)$$

where  $D_{50}$  is the mean particles size;  $\beta$  is an empirical parameter that controls the shape of the function. Note that we rewrite the formulation of cumulative distribution function in Eq. (4) based on the convention formulation [25], to relate the first parameter to a more physical-meaningful parameter  $D_{50}$ . A smaller  $\beta$  value yields a wider particle size distribution curve while a larger  $\beta$  value would yield a more narrow distribution. The fitted RR model to the experiment data of the JSC-1A MRS is shown in Fig. 3b and the model parameters  $D_{50} = 0.41$  mm and  $\beta = 0.75$ .

#### 4 Characterization of particle shapes

An equivalent important factor affecting the mechanical behavior of the regolith simulant is its particle shapes. In this work, an MILabs U-CT system with an optimal resolution of 100 micron is used to obtain X-ray computed tomography (CT) image data of individual particles within

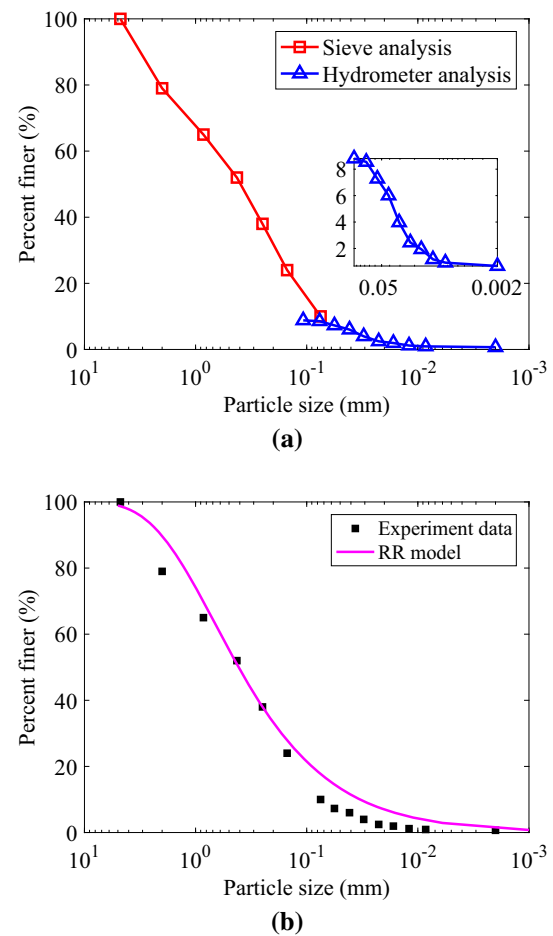


**Fig. 3** Particle size distribution of JSC-1A MRS: **a** data obtained from sieve and hydrometer analysis; **b** fitted by a Rosin–Rammler (RR) distribution model with model parameters  $D_{50} = 0.41$  mm,  $\beta = 0.75$

the regolith simulant specimen. Imaging processing algorithms are implemented to extract, quantify and characterize particles shape data, which is then used to develop shape-dependent discrete element models.

#### 4.1 X-ray computed tomography imaging and pre-processing

Figure 4 shows the regolith simulant, the specimen to be scanned, and a typical raw image obtained from CT scan.

The raw images obtained from CT scan require a series of pre-processing steps before they can be used to extract particle shapes. The pre-processing steps include image enhancement, vessel removal, smooth filtering and inner particle void filling [26].

The image enhancement is to enhance the contrast between the particle pixels and the background pixels. A contrast limited adaptive histogram equalization (CLAHE) [27] is implemented for this purpose. Vessel removal is to remove

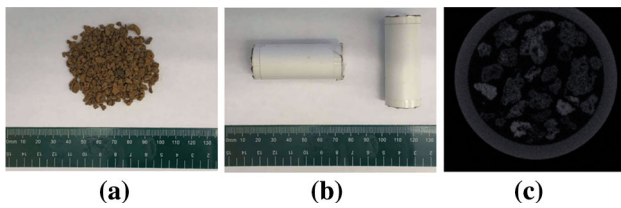


**Fig. 4** X-ray CT imaging experiment: **a** regolith simulant; **b** specimen to be scanned; **c** a typical raw image

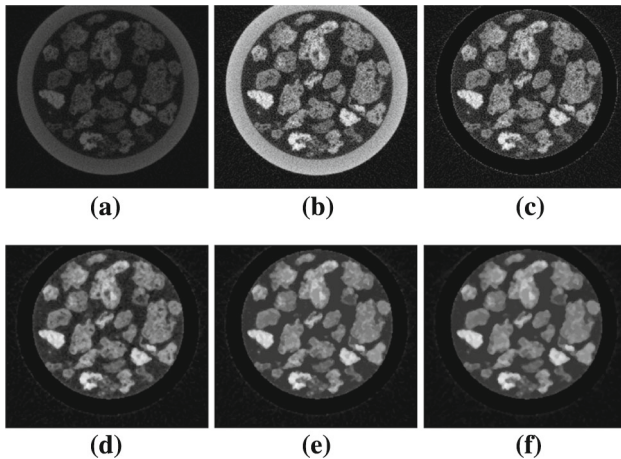


**Fig. 5** An illustration of the CT image pre-processing on a typical raw CT image. **a** Raw image, **b** image enhancement, **c** vessel removal, **d** smooth filtering, **e** filling voids, **f** smooth filtering

the column vessel containing the sample particles. Due to the perturbation of tomography environment and the limitation of CT optical apparatus, the CT image may contain significant noises. Therefore, a smooth filtering technique termed the median filter algorithm [28] is used to reduce the noise pixels. Finally, the inner particle voids, due to either imaging noise or actual voids within the particle, will be “filled” during pre-processing. The filling step is justified based on the fact that interactions between particles in the numerical model will be determined by the outer boundary of each particle only.

The image pre-processing steps can be used in combination to obtain optimal images for shape extraction. Figure 5 shows the pre-processing of a typical raw image. It should be pointed out that, no matter how advanced algorithms are used, there processed images may still pose unreasonable pixel values. Manual adjustment may be used to remove unnecessary pixels and to improve the image quality.

#### 4.2 Particle shape identification

Given a processed CT image, particle shapes will be identified and extracted. Three techniques are used for this purpose: component differentiation, watershed segmentation, and shape identification.

**Component differentiation** Component differentiation refers to classifying individual component of a specimen. It is based on the fact that different types of component have different X-ray attenuation coefficients, which can be further converted to grayscale images. Clustering algorithms, such as the K-mean clustering algorithm [29,30], can be applied to distinguish each component type in a sample. A particular case of the clustering analysis is binarization, where only two components need to be identified. An example is to identify the solid and void phases within a specimen, as is the case in this work.

**Watershed segmentation** The watershed segmentation algorithm [31] is commonly used to segregate individual particles. Watershed segmentation algorithm imitates a water flooding process, where water rises from a *local* minimum altitude and flows towards the *nearest* not-flooded minimum altitude. The floods rise from different *local* minimum altitude or basin would encounter and form a boundary between each basin, thus segregate each basin. In application, topographic distance field is computed from the binary image and used as the altitude in watershed segmentation.

**Shape identification** Shape identification is used to mark or label the segregated particles. After watershed segmentation, the particles will be segregated from each other by the watershed boundaries. Then, every particle pixels inside the same boundary can be marked and identified as a single particle. The general procedure outlined in [32] is commonly used.

It should be noted that, during the watershed segmentation, the image is required to be “eroded” by a topographic structure element. The size of the topographic structure element would impact the segregated particle shapes. If the element size is too small, the algorithm may not be able to identify two particles that are in touch. On the other hand, if the element size is too large, the algorithm may miss some smaller particles. In this work, the size of the topographic structure element is gradually increased. For each size, the watershed algorithm and shape identification are performed. The resulting image is sent to the next iteration until reasonable particle shapes are identified. Figure 6 illustrates the effects of each procedure in the algorithm. For this example, eight iterations are used to obtain the final image.

#### 4.3 Quantitative description of particle shapes

With particle shapes identified and extracted following techniques described in the previous section, it is possible to calculate quantitative descriptors of particle shapes within a specimen. In this work, three shape descriptors are calcu-



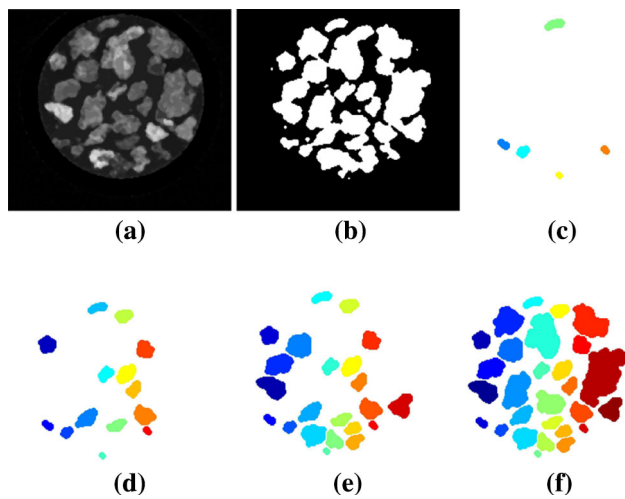


**Fig. 6** An illustration of particle identification from a pre-processed CT image. **a** After preprocessing, **b** image binarization, **c** watershed of 5th erosion, **d** watershed of 7th erosion, **e** watershed of 8th erosion, **f** final segments

lated, i.e., the Fourier harmonic descriptor, the aspect ratio, and the circularity.

**Fourier harmonic descriptor** When using the Fourier harmonic descriptor, the polar radius  $r$  of a particle is written as a function of the polar angle  $\theta$  through a series of Fourier harmonic functions such that [33,34]

$$r_N(\theta) = \frac{R_o}{2} + \sum_{n=1}^N [a_n \cos(n\theta) + b_n \sin(n\theta)] \quad (5)$$

where  $R_o$  is the equivalent particle diameter of a spherical or circular particle that has the same area as the irregular particle;  $N \geq 1$  is the Fourier series order;  $a_n$  and  $b_n$  (with  $n = 1, 2, 3, \dots, N$ ) are the Fourier coefficients defined as

$$a_n = \frac{1}{\pi} \int_0^{2\pi} [r(\theta) \cos(n\theta)] d\theta \quad (6)$$

$$b_n = \frac{1}{\pi} \int_0^{2\pi} [r(\theta) \sin(n\theta)] d\theta \quad (7)$$

In this work, Fourier coefficients are evaluated for a total of 297 particle shapes extracted from CT images. To compare between particles of different sizes, the coefficients ( $a_n$ ,  $b_n$ ) are normalized by the equivalent particle diameter  $R_o$ . Furthermore, a normalized mean amplitude is calculated as the square root of the sum of the normalized coefficients squared. The normalized amplitude versus the harmonic number plot is shown in Fig. 7, where the harmonic number  $n = 1, 2, 3, \dots, N$  and  $N = 15$  for this study.

**Aspect ratio** Aspect ratio is defined as the ratio of the short axis to the long axis. For a circular particle, the aspect ratio would be one. Figure 8a shows the aspect

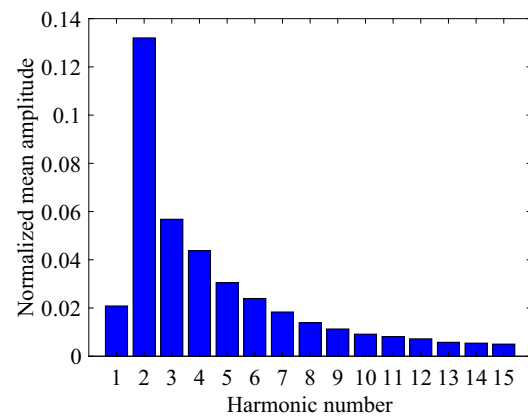


**Fig. 7** Fourier harmonic descriptor for all particle shapes extracted from CT images

ratio distribution of the particle shapes extracted from CT images. The mean aspect ratio is about 0.57.

**Circularity** Circularity describes the degree to which a particle shape is similar to a circle, and it is a measure of both the particle form and roughness [35]. The circularity of a particle is a dimensionless quantity given as [35]

$$C = \sqrt{\frac{4\pi A}{P^2}} \quad (8)$$

where  $A$  is the area of the particle;  $P$  is the perimeter defined as the total length of the particle boundary. A higher circularity value means the particle is closer to a perfectly round and smooth particle. An ellipse with an aspect ratio of 0.57 has a circularity of about 0.92. Figure 8b plots the histogram of the circularities of the scanned specimen. The mean circularity is about 0.86.

The particle shape descriptors can be used to generate numerical particle assembly that possesses similar shape properties of a corresponding physical particle assembly or to quantify the relationship between macroscopic material properties (e.g., shear strength) and particle shapes [36]. A more direct approach, as adopted in this work, is to generate particles with realistic irregular shapes using extracted particle shape data from CT images. In the next section, a subset of realistic particle shapes extracted from CT image will be used to illustrate the development of a grading and shape-dependent discrete element model.

## 5 Discrete element model

In this section, two-dimensional (2D) discrete element model will be developed to simulate the behavior of the JSC-1A MRS. The model explicitly accounts for particle size distribution and realistic irregular particle shapes extracted from CT

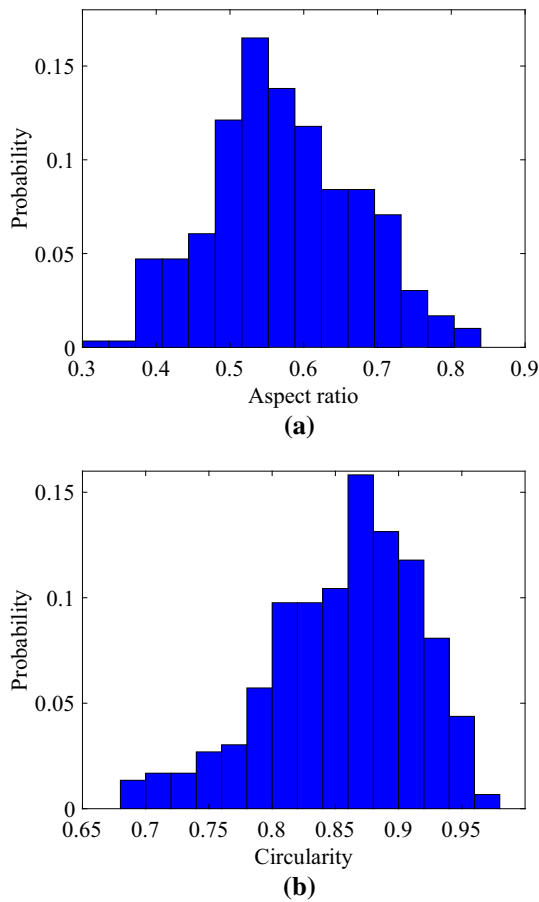


**Fig. 8** Particle shape descriptors of the extracted particle shapes. **a** Aspect ratio, **b** circularity

images. Despite the limitations of a 2D numerical model, the procedure presented for model development is general. The developed model can capture microscopic behavior between regolith particles and the responses of the system with reasonable computational time.

### 5.1 Contact models

In a discrete element model, the microscopic interactions between particles are simplified into contact behavior of two elements. The contact force  $\mathbf{F}_c$  consists of two parts: the normal force  $\mathbf{F}_n$  and the shear force  $\mathbf{F}_s$

$$\mathbf{F}_c = \mathbf{F}_n + \mathbf{F}_s = F_n \mathbf{n}_n + F_s \mathbf{n}_s \quad (9)$$

where  $\mathbf{n}_n$  and  $\mathbf{n}_s$  are the unit vectors denoting the direction of the normal and the shear force, respectively;  $F_n$  and  $F_s$  are the magnitudes of corresponding contact forces. Assuming the relative displacement increment at the contact during a timestep  $\Delta t$  is given by its components  $\Delta \delta_n$  and  $\Delta \delta_s$ , the contact law for a simple linear model updates the contact forces through

$$F_n = \max(F_n^0 + k_n \Delta \delta_n, 0) \quad (10)$$

$$F_s = \min(F_s^0 + k_s \Delta \delta_s, \mu_c F_n) \quad (11)$$

$$M = 0 \quad (12)$$

where  $F_n^0$  and  $F_s^0$  are the normal and the shear force at the beginning of the current timestep, respectively;  $k_n$  and  $k_s$  are the normal and the shear stiffness, respectively;  $\mu_c$  is the microscopic friction coefficient, and  $M$  is the contact moment.

In Eq. (11), an incremental displacement formulation is used to calculate the tangential force to avoid the “ghost force” issue when the accumulative shear displacement is too large and needs a long time for relaxation during the simulation. Alternatively, a modification of the original Cundall and Strack [17] force was proposed by [37] and adopted in [38], which “freezes” the shear displacement when the shear force reaches a given threshold.

A more complex contact law may include rolling resistance such as the one proposed in [39,40], where a term of rolling resistance moment is added to the contact moment as

$$M = \min(M^0 + k_r \Delta \theta_b, \mu_r \bar{R} F_n) \quad (13)$$

where  $M^0$  is the contact moment at the beginning of the current timestep;  $\Delta \theta_b$  is the relative bend-rotation increment;  $\mu_r$  is the rolling resistance coefficient;  $k_r$  is the rolling resistance stiffness defined as:

$$k_r = k_s \bar{R}^2 \quad (14)$$

where  $\bar{R}$  is the contact effective radius defined as  $\bar{R} = 1/(\frac{1}{R_1} + \frac{1}{R_2})$ , in which  $R_1$  and  $R_2$  are the radii of the contact particles. If one side of the contact is a wall, the corresponding radius  $R_2 \rightarrow \infty$ .

It should be noted that the adopted rolling resistance model of Eq. (13) uses a simplified formulation for the rolling kinematics, and the particle size effects on the rolling resistance are implicitly incorporated in the rolling stiffness term. The interested reader is referred to [41,42] for examples of improved and more advanced rolling resistance models.

The rolling resistance model can be used to indirectly account for effects of irregular particle shapes and to improve predictions of a discrete element model with only circular particles. As a comparison, discrete element models with circular particles and rolling resistance will also be implemented and compared with the shape-dependent model.

### 5.2 Particle size distribution

In a discrete element simulation, the computational cost is positively correlated to the number of particles in the model. Though the MRS contains only a small amount of fine particles (less than 10% by weight), the number of fine particles

can be prohibitively large. When setting up a discrete element model, within the limits of the current computational resources, it may become necessary to introduce some reasonable approaches to modify the particle size distribution, so that the total number of particles can be reduced. Two approaches can be used to reduce the number of particles: up-scaling of particle sizes [43–45], and modifying the gradation by trimming fine particles.

For soil samples with a broad range of particle sizes like the MRS, up-scaling of particle sizes may not be appropriate: a small scaling factor could be insufficient to significantly reduce the number of particles, and a large scaling factor might result in unrealistically large particles. With the trimming approach, fine contents are considered to have negligible contributions to the mechanical strength of the sample, and therefore, they can be “trimmed” or removed.

Considering the wide range of particle sizes and the powder-like tiny particles in the MRS, the particle trimming method is adopted to reduce the particle number in this work. For the particles that are smaller than 0.425 mm, they are substituted with alternative particles whose size are equal to 0.425 mm. However, the number of alternative particles will be recalculated so that the resulting particle packing has the same volume fraction as the original specimen.

### 5.3 Particle shape representation

Many methods have been proposed and developed to simulate irregularly-shaped particles, e.g., the disc clump method [33,46], the spheropolygon (2D) and spheropolyhedron (3D) method [47,48], the polyhedrons method [49,50], the non-uniform rational basis splines method [51], the level set method [52] and so on. In this work, an irregularly-shaped particle is modeled using a group of discs called a clump. The most notable advantages of this method are its computational efficiency and straightforward implementation of contact detection algorithms. There are three options to represent a clump [46]: the domain overlapping filling method, the domain non-overlapping filling method, and the boundary filling method, as shown in Fig. 9. The clump generated by domain overlapping filling requires the least number of particles and is, therefore, the most computationally efficient. The clump created by the domain non-overlapping filling can also be promoted to a cluster that can capture the breakage behavior. The boundary filling method, depending on the size of filling elements, could provide a better representation of surface roughness.

The domain overlapping filling method is adopted in this work. This approach is also called the Overlapping Discrete Element Cluster (ODEC) method, and the filling process consists of three main steps [33]: image matrix parameterization, topological skeletonization, and optimum overlapping, as illustrated in Fig. 10. It should be noted that the irregularly-

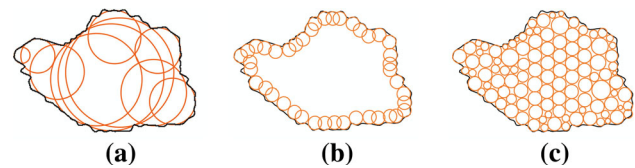


**Fig. 9** Schematic illustration of the three options for representing an irregularly-shaped MRS particle with disc clump method (modified after [46]). **a** Domain overlapping, **b** boundary filling, **c** domain nonoverlapping filling

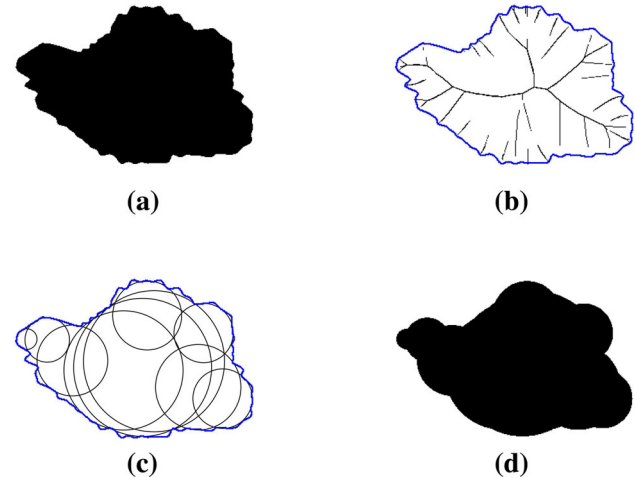


**Fig. 10** Schematic illustration of particle shape representation using the domain overlapping filling method. **a** Binary image matrix, **b** topological skeleton, **c** optimum overlapping, **d** resultant clump

shaped particles generated by the ODEC method are actually clumps (those that do not break), but the phrase ODEC is kept in this work as it was originally used in [33].

In the image matrix parameterization, the particle shape is converted to binary image matrix, with status labels indicating particle pixels and background pixels. The binary images are collections of binary pixels that signal whether a square area (or a cubic volume in 3D) is occupied by solid ( $b = 1$ ) or by void ( $b = 0$ ). Topological skeletonization, or Medial Axis Transformation, is used to identifying skeleton of a particle, which is defined as the locus of centers of all maximally inscribed discs. In optimum overlapping, discs are iteratively added to the clump. For each iteration, the center of the new discs to be added is searched on the topological skeleton, and it is assured that the newly added disc can cover the maximum uncovered area.

When applying the ODEC algorithm to irregularly-shaped particles (i.e. non-circular or non-spherical particles), as the number of discs used per clump increases, the percentage of covered area also increases. Figure 11 shows the relation of the percentage coverage and the number of discs per clump based on CT image data of the MRS. A clump with a larger number of discs would have a better representation of the particle shape but with higher computational cost. In this



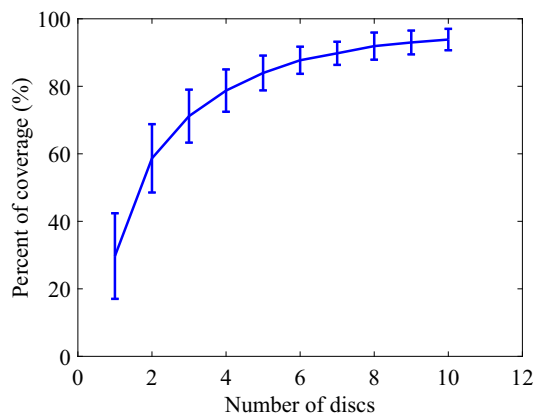


**Fig. 11** The percentage coverage as a function of discs number in the domain overlapping filling method. The *error bars* indicate the variation of the percentage coverage among different particle shapes when the same number of discs are used



**Fig. 12** Seven basic particle shapes used in the DEM model

work, each clump is filled by five discs, corresponding to an 80% area coverage. Each clump represents an irregularly-shaped particle.

In the following analysis, seven irregular particle shapes are selected and, therefore, there are seven clump templates used in developing the discrete element model. These seven shape templates are shown in Fig. 12. The seven types of particle shapes are imported into the discrete element model as clump templates. Each generated particle in DEM model is based on a randomly selected clump template with its size following the particle size distribution described in the previous subsection.

## 6 DEM simulation of direct shear tests

### 6.1 Model details and material parameters

The grading and shape-dependent DEM model is used to simulate direct shear tests on JSC-1A MRS. PFC2D [53] is used to implement the model and to perform simulations. The dimension of the soil specimen is 63.5 mm in width and 25.4 mm in height. The porosity of the packing in the DEM model is 0.22, which corresponds approximately to a porosity of 0.49 in a three-dimension sample following the parabolic equation recommended by [54].

To generate a numerical specimen following the prescribed particle size distribution with irregularly-shaped particles, the following steps are taken:

1. The particle size distribution (PSD) curve is first divided into a number of bins. In this work, the number of bins and bin sizes are set based on the number of sieves and sieve openings used in the laboratory sieve analysis.
2. The area of particles in each bin is calculated based on the total volume of the specimen and the target porosity.
3. Within each PSD bin, a particle size is randomly generated and the corresponding particle shape is randomly selected from the list of irregularly-shaped particles, e.g., Fig. 12.
4. The previously generated particle is scaled such that its area equals to the area of an equivalent disc with the same particle size.
5. The scaled irregularly-shaped particle is then inserted to the specimen at a randomly selected position.
6. Steps 3–5 are repeated for each PSD bin until the total area of the generated particles matches the target area computed in step 2.
7. The generated specimen is allowed to settle under gravity.

It is worth noting that, within the limits of the resolution of the X-ray CT system, the particle shapes at different particle sizes are not directly obtained. Herein, the particle shape or shape descriptors are assumed to resemble each other at different sizes, known as the fractal phenomenon of granular material [55]. Therefore, the same shape templates are used at different scales in generating the numerical specimen.

The generated numerical specimen is shown in Fig. 13. During the preparation of soil specimen in the laboratory test, the specimen is vibrated and slightly compacted to remove potential cavity and improve sample homogeneity. In the numerical simulation, for the same purpose and during the specimen preparation stage, the shearing cell is set to be frictionless, and the friction coefficient of soil particles is set to be 0.1. The input parameters for the DEM model are calibrated using one set of laboratory test data corresponding to a confining stress of 95.8 kPa, following a calibration procedure

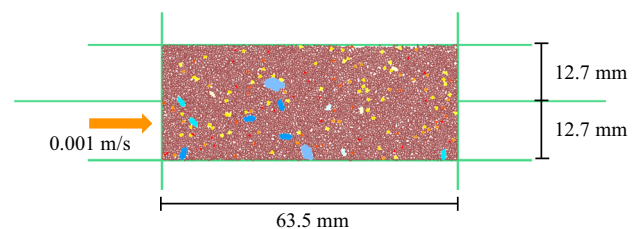


**Fig. 13** Discrete element model of a direct shear test specimen. *Light green lines* represent the shearing cell and different *colors* are used to indicate particles with different sizes (color figure online)

**Table 3** Input parameters for the DEM model

Parameter	Value
Width of shear cell $w$	63.5 (mm)
Height of shear cell $h$	25.4 (mm)
Packing porosity $\phi$	0.22
Density of particles $\rho$	1940 (kg/m <sup>3</sup> )
Contact normal stiffness $k_n$ *	$1.5 \times 10^7$ (N/m)
Contact shear stiffness $k_s$ *	$1.5 \times 10^7$ (N/m)
Friction coefficient of particles $\mu_c^b$ *	2.5
Friction coefficient of boundary $\mu_c^w$ *	2.0
Rolling resistance coefficient $\mu_r$ **	0.7

\* Denotes the parameters that need to be calibrated.

\*\* Is the rolling resistance coefficient required if using simplified disc only particles with the rolling resistance contact model to account for particle shape irregularity

similar to [56–58]. The calibrated values are summarized in Table 3. Then, the other sets of test data are used to validate simulation results of the DEM model.

The direct shear test consists of two stages: consolidation and shearing. In the numerical simulation, the movement of the shearing cell is governed by servo-control mechanism [53] to achieve and maintain a specified consolidation pressure. Three different confining stresses, i.e., 95.8, 191.5 and 383 kPa, are considered. The time step is set at  $2 \times 10^{-6}$  s. In the shearing stage, the lower part of the shearing cell is moved at a speed of 0.001 m/s. The simulation is stopped when the normalized shear displacement reaches 12% or the shear stress reaches its peak and significantly decreases.

## 6.2 Results and discussion

Figure 14a shows the shear stress and shear displacement behavior of the MRS in the direct shear test. The results

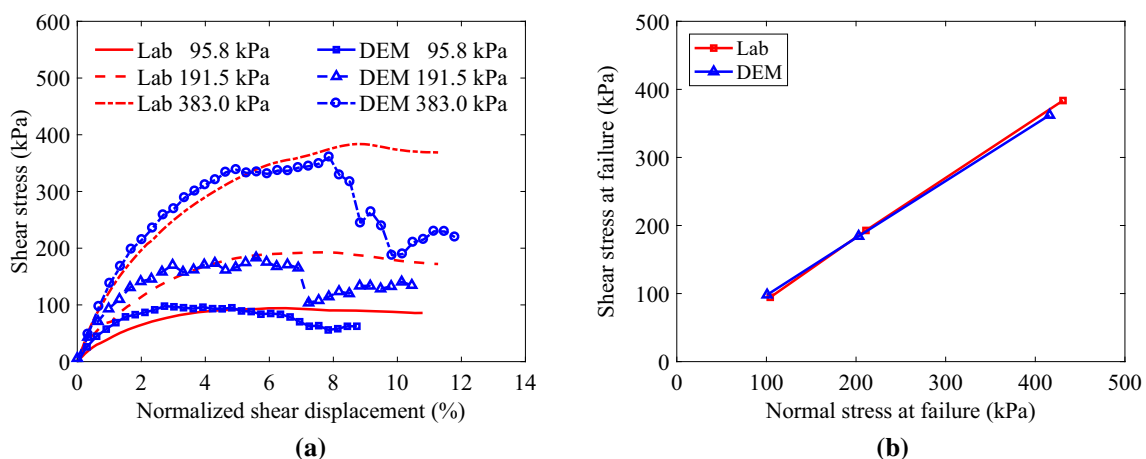
from the developed discrete element model match reasonably well with the experimental data, and the peak shear stress can be perfectly captured. The shear stress from DEM model exhibits a more significant decrease in the post-peak stage compared to the laboratory experiment. The post-peak difference between the DEM and experiment results, as being previously observed in [44,45], may come from the particle breakage effect that is not included in the DEM model. In addition, the simplification of a 3D problem into a 2D DEM model also contributes to the differences. Nevertheless, the DEM simulation predicts a maximum macroscopic friction angle of  $40^\circ$ , which matches very well with the value obtained from lab test ( $41.4^\circ \pm 2.2^\circ$ ).

As a comparison, two additional cases of DEM simulations are performed. The first case uses the same input parameters for the linear contact law and the same gradation but with simple disc-shaped particles, i.e., no consideration of particle shapes. The second case also uses disc-shaped particles but incorporates the rolling resistance model of Eq. (13).

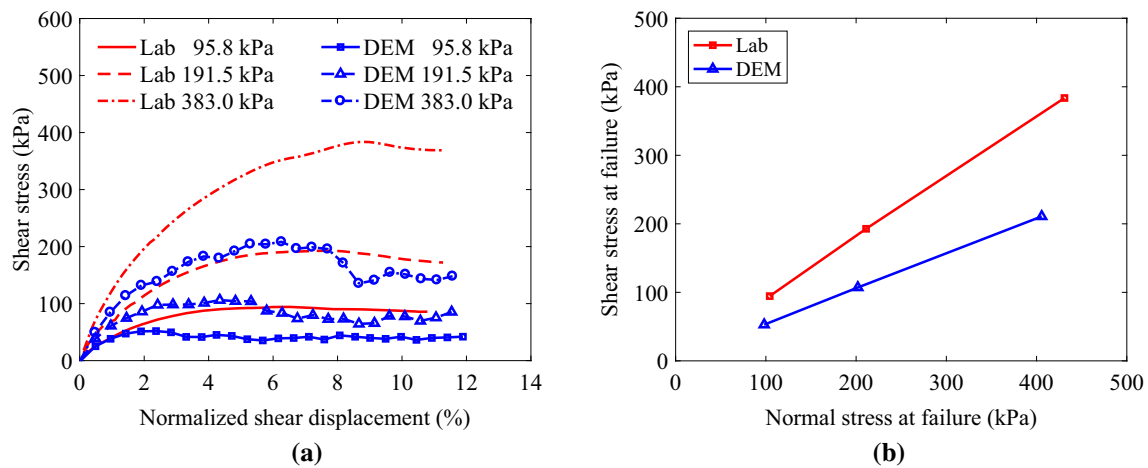
Figure 15 shows stress responses of DEM simulation with disc-shaped particles. For such a case, the maximum macroscopic friction angle is  $27.2^\circ$ , and the corresponding friction coefficient is about 40% less than the value obtained with shape-dependent DEM simulations. This comparison shows that the particle shape irregularity makes a significant contribution to the shear strength of this material.

Figure 16 plots the stress responses of disc-shaped particles with the rolling resistance model of Eq. (13). In this case, a rolling resistance coefficient  $\mu_r$  of 0.7 is required to achieve the same shear strength predicted using the shape-dependent DEM model.

Figure 17 shows the formation and evolution of shear band (characterized by particle rotations) for all three cases of DEM simulations. Two main distinct effects of particle



**Fig. 14** Grading and shape-dependent DEM simulations of direct shear test: stress response and comparison with laboratory test. **a** Stress displacement behavior, **b** normal and shear stress at failure



**Fig. 15** DEM simulations of direct shear test with disc-shaped particles and a linear contact model: stress response and comparison with laboratory test. **a** Stress displacement behavior, **b** normal and shear stress at failure

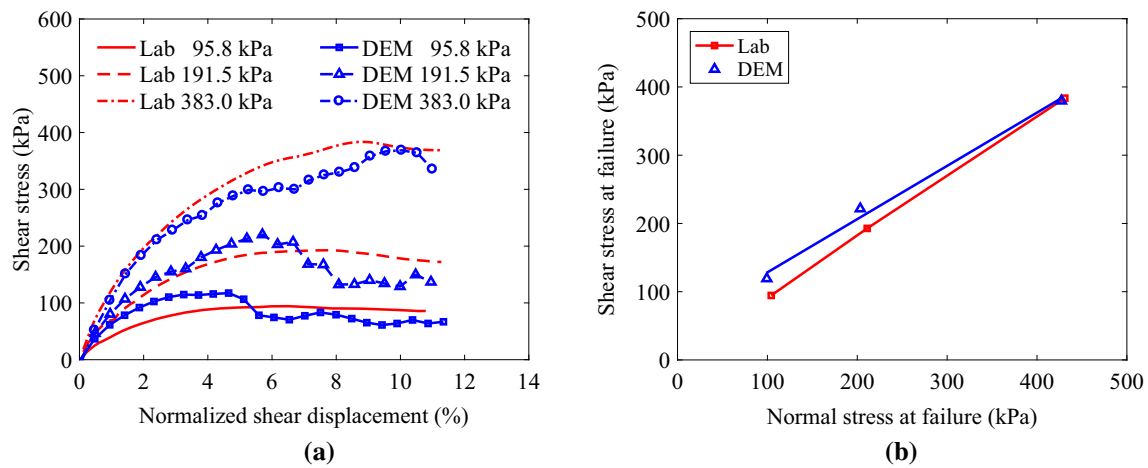


**Fig. 16** DEM simulations of direct shear test with disc-shaped particles and a rolling resistance contact model: stress response and comparison with laboratory test. **a** Stress displacement behavior, **b** normal and shear stress at failure

shape irregularity on the shear band can be observed: (1) the particle shape irregularity tends to resist or inhibit the shear band formation; and (2) the particle shape irregularity could induce additional shear band in a direction other than the common horizontal direction.

Previous study [36] has found that particle shape irregularity could increase the coordination number and increase the mobilized particle contact friction, leading to a larger macroscopic friction angle. A similar phenomenon is captured by the grading and shape-dependent DEM model developed in this work. Here, the coordination number can be directly related to the total contact number in the model, since the particle number in DEM specimens are the same. Figure 18 shows the polar histogram of the contact force directions in the specimens at peak shear stress state with a normal stress of 95.8 kPa. It can be observed that the specimen with irregularly-shaped particles possesses the largest number of

contacts. It is also interesting to note the anisotropic nature of the contact network for three different cases, which could affect the macroscopic material response. For instance, the dependence of elastic constants on the contact network has been reported and quantified in [59]. The contact forces directed close to horizontal give a higher shearing resistance in the direct shear test. The contact force directions cluster around  $30^\circ$  for the specimen with irregularly-shaped particles and the specimen with discs and rolling resistance. The contact force directions cluster around  $45^\circ$  for the specimen with disc-shaped particles and no rolling resistance. Results of the mobilized contact friction in each specimen are shown in Fig. 19. Consistent with the previous study [36], the specimen with irregularly-shaped particles possesses the largest percentage of mobilized particle contact friction that is greater than the macroscopic friction ( $\tan 40^\circ$ ).

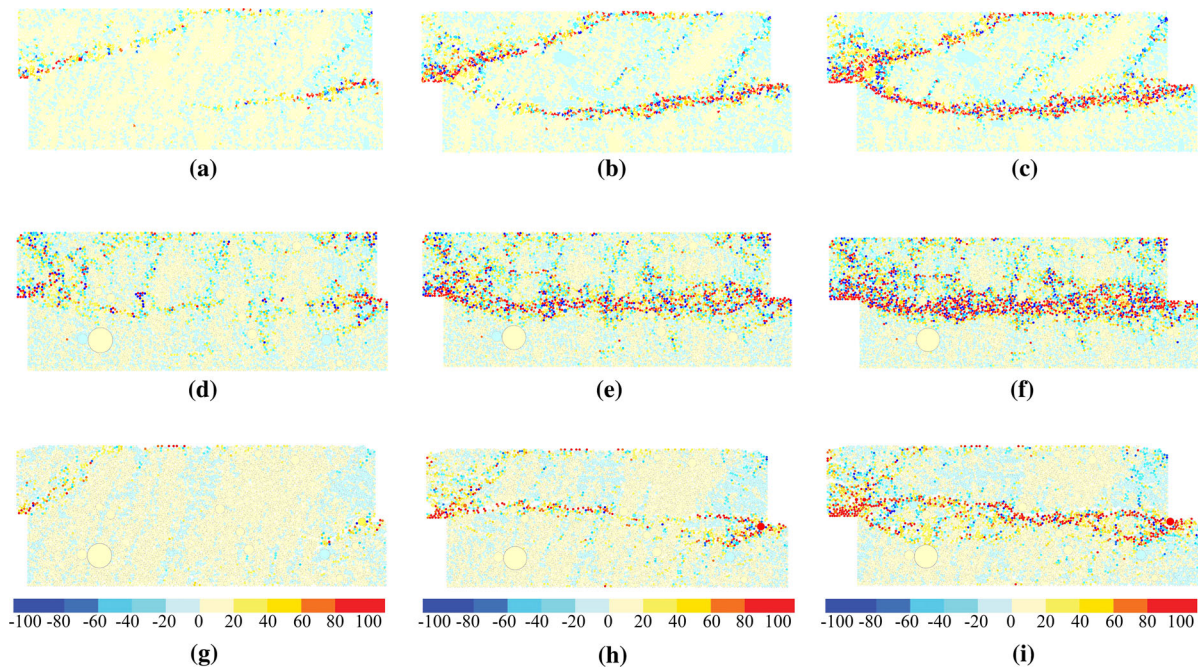


**Fig. 17** Shear band in numerical DST at 3, 6 and 9% shearing displacement with normal stress 95.8 kPa. The *color* indicates the rotation of the particle. The unit of the *color bar* is in degree with a counterclockwise rotation being positive. **a** Irregular particles, 3%, **b** irregular particles,

6%, **c** irregular particles, 9%, **d** disc particles, 3%, **e** disc particles, 6%, **f** disc particles, 9%, **g** discs with rolling resistance, 3%, **h** discs with rolling resistance, 6%, **i** discs with rolling resistance, 9% (color figure online)

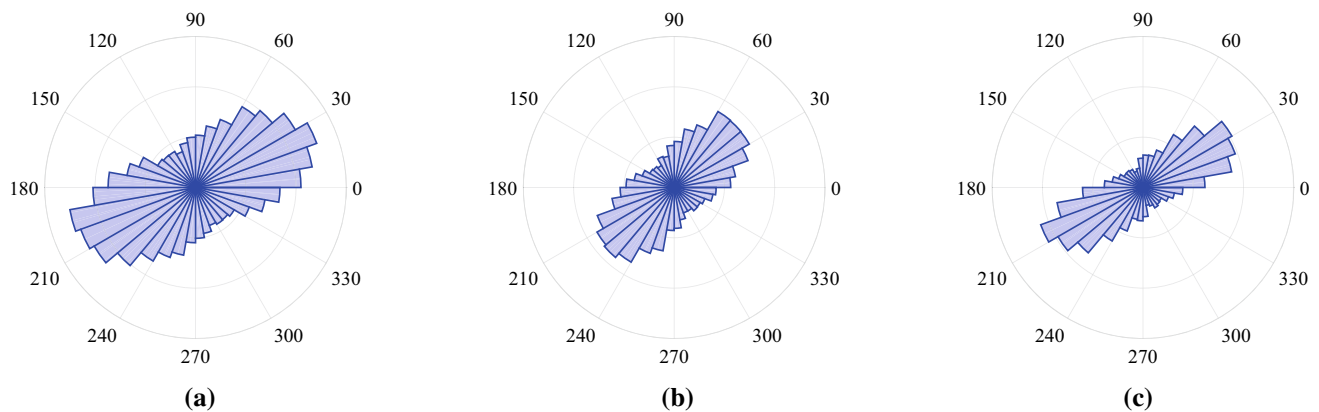


**Fig. 18** Polar histogram of the contact direction at peak shear stress with a normal stress of 95.8 kPa. **a** Irregular particles, **b** disc particles, **c** discs with rolling resistance

## 7 Conclusions

In this work, the physical and mechanical properties of JSC-1A MRS are characterized by a series of laboratory tests. The properties characterized include specific gravity, particle size, particle size distribution, particle shapes and shear strength. X-ray computed tomography is used to obtain particle images, upon which particle shape data are characterized by a series of imaging processing techniques and are further used to generate irregularly-shaped numerical particles through the domain overlapping filling method. A grading and shape-dependent DEM model is then developed, cali-

brated and validated against direct shear tests on JSC-1A MRS. In summary, it is found that

1. The JSC-1A MRS used in this study can be characterized as well-graded sand (SW) following the Unified Soil Classification System with a specific gravity of  $1.94 \pm 0.02$ .
2. The calibrated grading and shape-dependent DEM model can capture the behavior of the regolith simulant in a direct shear test, in particular, the peak shear strength and the maximum friction angle.
3. The particle shape effect accounts for approximately 40% of the shear resistance of the JSC-1A MRS. The irregular



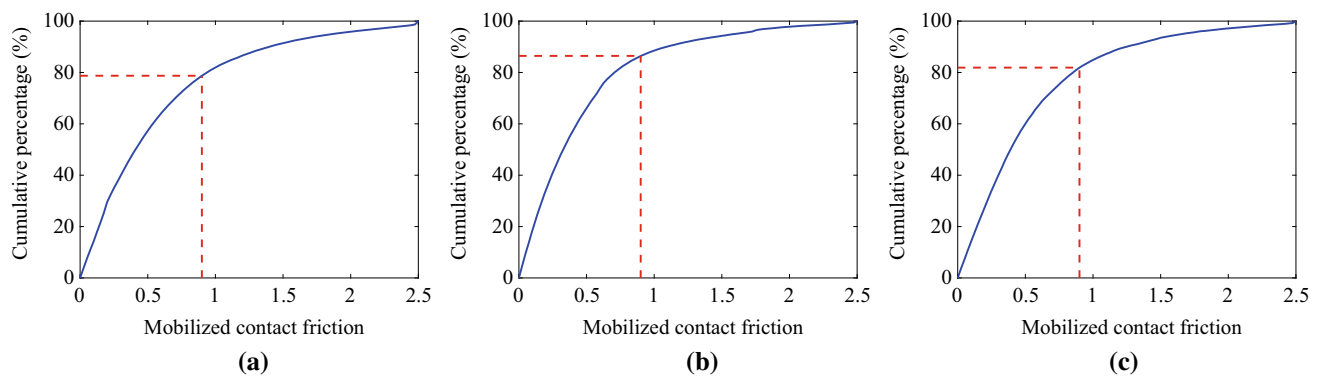


**Fig. 19** Cumulative frequency of mobilized contact friction coefficient for all contacts at peak shear stress with a normal stress of 95.8 kPa. The red dashed line indicates the mobilized contact friction corresponding to

$\tan 40^\circ$ , where  $40^\circ$  is the maximum macroscopic friction angle obtained from DEM simulations with irregular particles. **a** Irregular particle, **b** disc particles, **c** discs with rolling resistance (color figure online)

particles would increase the mobilized contact friction and the number of particle contacts within the assembly when compared with an assembly with the same number of disc-shaped particles.

4. The additional shear resistance resulting from irregular particle shape effect cannot be fully replicated by solely increasing the micro friction between particles but can be captured through a calibration of rolling resistance contact model.

The laboratory characterization and numerical model developed in this work provide insights into the mechanical behavior of JSC-1A MRS from a fundamental level. The calibrated grading and shape-dependent model can be a useful tool for simulating and predicting regolith behavior in a complex environment such as microgravity and low pressure, which will be explored in future studies.

**Acknowledgements** The authors would like to acknowledge the financial support provided by the NASA SC Space Consortium Grants (Grant Nos. 521179-RP-CMChen and 521179-PA-CMChen2).

#### Compliance with ethical standards

**Conflict of interest** The authors declare that they have no conflict of interest.

## References

1. Iagnemma, K., Shibly, H., Dubowsky, S.: A laboratory single wheel testbed for studying planetary rover wheel–terrain interaction. MIT field and space robotics laboratory Technical Report, **1**, 05–05 (2005)
2. Sullivan, R., Anderson, R., Biesiadecki, J., Bond, T., Stewart, H.: Cohesions, friction angles, and other physical properties of Martian regolith from mars exploration rover wheel trenches and wheel scuffs. *J. Geophys. Res. Planets* **116**(E2), E02006 (2011)
3. Ding, L., Gao, H., Deng, Z., Nagatani, K., Yoshida, K.: Experimental study and analysis on driving wheels' performance for planetary exploration rovers moving in deformable soil. *J. Terramech.* **48**(1), 27–45 (2011)
4. Carranza, S., Makel, D.B., Blizman, B., El-Genk, M.S.: In situ manufacturing of plastics and composites to support H&R exploration. In: AIP Conference Proceedings, vol 813, pp. 1122–1129. AIP, (2006)
5. Sen, S., Carranza, S., Pillay, S.: Multifunctional Martian habitat composite material synthesized from in situ resources. *Adv. Space Res.* **46**(5), 582–592 (2010)
6. Wan, L., Wendner, R., Cusatis, G.: A novel material for in situ construction on Mars: experiments and numerical simulations. *Constr. Build. Mater.* **120**, 222–231 (2016)
7. Moses, R.W., Bushnell, D.M.: Frontier in-situ resource utilization for enabling sustained human presence on mars. Technical Report NASA-TM-2016-219182, NASA Langley Research Center (2016)
8. Allen, C.C., Jager, K.M., Morris, R.V., Lindstrom, D.J., Lindstrom, M.M., Lockwood, J.P.: JSC Mars-1: a Martian soil simulant. In: Space 98, pp. 469–476. American Society of Civil Engineers (1998)
9. Brunskill, C., Patel, N., Gouache, T.P., Scott, G.P., Saaj, C.M., Matthews, M., Cui, L.: Characterisation of martian soil simulants for the ExoMars rover testbed. *J. Terramech.* **48**(6), 419–438 (2011)
10. Gouache, T.P., Patel, N., Brunskill, C., Scott, G.P., Saaj, C.M., Matthews, M., Cui, L.: Soil simulant sourcing for the ExoMars rover testbed. *Planet. Space Sci.* **59**(8), 779–787 (2011)
11. Peters, G.H., Abbey, W., Bearman, G.H., Mungas, G.S., Smith, J.A., Anderson, R.C., Douglas, S., Beegle, L.W.: Mojave Mars simulant—characterization of a new geologic Mars analog. *Icarus* **197**(2), 470–479 (2008)
12. Scott, A.N., Oze, C., Tang, Y., O'Loughlin, A.: Development of a Martian regolith simulant for in-situ resource utilization testing. *Acta Astronautica* **131**, 45–49 (2017)
13. Zeng, X., Li, X., Wang, S., Li, S., Spring, N., Tang, H., Li, Y., Feng, J.: JMSS-1: a new Martian soil simulant. *Earth Planets Space* **67**(1), 1–10 (2015)
14. Tu, X., Andrade, J.E., Chen, Q.: Return mapping for nonsmooth and multiscale elastoplasticity. *Comput. Methods Appl. Mech. Eng.* **198**(30), 2286–2296 (2009). doi:10.1007/s11440-013-0276-x
15. Chen, Q., Andrade, J., Samaniego, E.: AES for multiscale localization modeling in granular media. *Comput. Methods Appl. Mech. Eng.* **200**(33), 2473–2482 (2011)
16. Andrade, J.E., Chen, Q., Le, P.H., Avila, C.F., Evans, T.M.: On the rheology of dilative granular media: bridging solid-and fluid-like behavior. *J. Mech. Phys. Solids* **60**(6), 1122–1136 (2012). doi:10.1016/j.jmps.2012.02.011



17. Cundall, P.A., Strack, O.D.L.: A discrete numerical model for granular assemblies. *Géotechnique* **29**(1), 47–65 (1979)
18. Hopkins, M.A., Johnson, J.B., Sullivan, R.: Discrete element modeling of a rover wheel in granular material under the influence of Earth, Mars, and Lunar gravity. In: *Earth & Space 2008: Engineering, Science, Construction, and Operations in Challenging Environments*, pp. 1–7. American Society of Civil Engineers, (2008)
19. Hopkins, M.A., Knuth, M.A., Green, A.: Discrete element method simulations of digging in JSC-1A. In: *Earth and Space 2012: Engineering, Science, Construction, and Operations in Challenging Environments*, pp. 65–73. American Society of Civil Engineers (2012)
20. Knuth, M.A., Johnson, J.B., Hopkins, M.A., Sullivan, R.J., Moore, J.M.: Discrete element modeling of a Mars Exploration Rover wheel in granular material. *J. Terramech.* **49**(1), 27–36 (2012)
21. Johnson, J.B., Kulchitsky, A.V., Duvoy, P., Iagnemma, K., Senatore, C., Arvidson, R.E., Moore, J.: Discrete element method simulations of Mars Exploration Rover wheel performance. *J. Terramech.* **62**, 31–40 (2015)
22. Smith, W., Peng, H.: Modeling of wheel–soil interaction over rough terrain using the discrete element method. *J. Terramech.* **50**(5), 277–287 (2013)
23. Simoni, A., Houslsby, G.T.: The direct shear strength and dilatancy of sand-gravel mixtures. *Geotech. Geol. Eng.* **24**(3), 523–549 (2006)
24. Rosin, P., Rammler, E.: The laws governing the fineness of powdered coal. *J. Inst. Fuel* **7**, 29–36 (1933)
25. Allaire, S.E., Parent, L.E.: Size guide number and Rosin–Rammler approaches to describe particle size distribution of granular organic-based fertilisers. *Biosyst. Eng.* **86**(4), 503–509 (2003)
26. Soille, P.: *Morphological Image Analysis: Principles and Applications*. Springer, Berlin (2013)
27. Zuiderveld, K.: Contrast limited adaptive histogram equalization. In: Heckbert, P.S. (ed.) *Graphics Gems IV*, pp. 474–485. Academic Press Professional Inc, San Diego (1994)
28. Lim, J.S.: *Two-Dimensional Signal and Image Processing*. Prentice-Hall Inc, Upper Saddle River (1990)
29. Faber, V.: *Clustering and the Continuous k-means Algorithm*. Los Alamos Sci. **22**, 138–144 (1994)
30. Chen, C., Luo, J., Parker, K.J.: Image segmentation via adaptive K-mean clustering and knowledge-based morphological operations with biomedical applications. *IEEE Trans. Image Process.* **7**(12), 1673–1683 (1998)
31. Meyer, F.: Topographic distance and watershed lines. *Signal Process.* **38**(1), 113–125 (1994)
32. Haralock, R.M., Shapiro, L.G.: *Computer and Robot Vision*. Addison-Wesley Longman Publishing Co., Inc., Boston (1991)
33. Das, N.: *Modeling three-dimensional shape of sand grains using discrete element method*. PhD thesis, University of South Florida, (2007)
34. Mollon, G., Zhao, J.: Fourier–Voronoi-based generation of realistic samples for discrete modelling of granular materials. *Granular Matter* **14**(5), 621–638 (2012)
35. Olson, E.: Particle shape factors and their use in image analysis-part 1: theory. *J. GXP Compliance* **15**(3), 85 (2011)
36. Härtl, J., Ooi, J.Y.: Numerical investigation of particle shape and particle friction on limiting bulk friction in direct shear tests and comparison with experiments. *Powder Technol.* **212**(1), 231–239 (2011)
37. Brendel, L., Dippel, S.: *Lasting contacts in molecular dynamics simulations. Physics of Dry Granular Media*, pp. 313–318. Springer, Berlin (1998)
38. Alonso-Marroquín, F., Herrmann, H.J.: Calculation of the incremental stress–strain relation of a polygonal packing. *Phys. Rev. E* **66**(2), 021301 (2002)
39. Iwashita, K., Oda, M.: Rolling resistance at contacts in simulation of shear band development by DEM. *J. Eng. Mech.* **124**(3), 285–292 (1998)
40. Jiang, M., Yu, H., Harris, D.: A novel discrete model for granular material incorporating rolling resistance. *Comput. Geotech.* **32**(5), 340–357 (2005)
41. Luding, S.: Cohesive, frictional powders: contact models for tension. *Granular matter* **10**(4), 235–246 (2008)
42. Wang, Y., Alonso-Marroquín, F., Xue, S., Xie, J.: Revisiting rolling and sliding in two-dimensional discrete element models. *Particuology* **18**, 35–41 (2015)
43. Kim, B.S., Park, S.W., Kato, S.: DEM simulation of collapse behaviours of unsaturated granular materials under general stress states. *Comput. Geotech.* **42**, 52–61 (2012)
44. Wang, Z., Jacobs, F., Ziegler, M.: Visualization of load transfer behaviour between geogrid and sand using PFC<sup>2D</sup>. *Geotext. Geomembr.* **42**(2), 83–90 (2014)
45. Feng, K., Montoya, B.M., Evans, T.M.: Discrete element method simulations of bio-cemented sands. *Comput. Geotech.* **85**, 139–150 (2017)
46. Shi, C., Li, D., Xu, W., Wang, R.: Discrete element cluster modeling of complex mesoscopic particles for use with the particle flow code method. *Granular Matter* **17**(3), 377–387 (2015)
47. Dobrohotoff, P.B., Azeezullah, S.I., Maggi, F., Alonso-Marroquín, F.: Optimal description of two-dimensional complex-shaped objects using spheropolygons. *Granular Matter* **14**, 651–658 (2012)
48. Alonso-Marroquín, F., Wang, Y.: An efficient algorithm for granular dynamics simulations with complex-shaped objects. *Granular Matter* **11**(5), 317–329 (2009)
49. Mack, S., Langston, P., Webb, C., York, T.: Experimental validation of polyhedral discrete element model. *Powder Technol.* **214**(3), 431–442 (2011)
50. Govender, N., Wilke, D.N., Kok, S., Els, R.: Development of a convex polyhedral discrete element simulation framework for NVIDIA Kepler based GPUs. *J. Comput. Appl. Math.* **270**, 386–400 (2014)
51. Andrade, J.E., Lim, K.W., Avila, C.F., Vlahinić, I.: Granular element method for computational particle mechanics. *Comput. Methods Appl. Mech. Eng.* **241**, 262–274 (2012)
52. Kawamoto, R., Ando, E., Viggiani, G., Andrade, J.E.: Level set discrete element method for three-dimensional computations with triaxial case study. *J. Mech. Phys. Solids* **91**, 1–13 (2016)
53. Itasca Consulting Group, Inc. PFC – Particle Flow Code, Ver. 5.0, (2014). Minneapolis: Itasca
54. Wang, Z., Ruiken, A., Jacobs, F., Ziegler, M.: A new suggestion for determining 2D porosities in DEM studies. *Geomech. Eng.* **7**(6), 665–678 (2014)
55. Arasan, S., Akbulut, S., Hasiloglu, A.S.: The relationship between the fractal dimension and shape properties of particles. *KSCE J. Civil Eng.* **15**(7), 1219–1225 (2011)
56. Belheine, N., Plassiard, J.P., Donzé, F.V., Darve, F., Seridi, A.: Numerical simulation of drained triaxial test using 3D discrete element modeling. *Comput. Geotech.* **36**(1), 320–331 (2009)
57. Plassiard, J.P., Belheine, N., Donzé, F.V.: A spherical discrete element model: calibration procedure and incremental response. *Granular Matter* **11**(5), 293–306 (2009)
58. Behraftar, S., Galindo Torres, S.A., Scheuermann, A., Williams, D.J., Marques, E.A.G., Janjani Avarzaman, H.: A calibration methodology to obtain material parameters for the representation of fracture mechanics based on discrete element simulations. *Comput. Geotech.* **81**, 274–283 (2017)
59. Alonso-Marroquín, F., Luding, S., Herrmann, H.J., Vardoulakis, I.: Role of anisotropy in the elastoplastic response of a polygonal packing. *Phys. Rev. E* **71**(5), 051304 (2005)